

Liquid-crystalline chiral phase formation and structural transitions of dumbbell-shaped colloids

Yang Yang

University of Maryland <https://orcid.org/0000-0002-0638-4274>

Guangdong Chen

University of Maryland

Hanwen Pei

Jilin University,

Xuefei Zhang

Fudan University

Wei Shi

Beihang University

Mingjie Liu

Beihang University

Charl Faul

University of Bristol <https://orcid.org/0000-0001-6224-3073>

Bai Yang

Jilin University <https://orcid.org/0000-0003-1939-6423>

Zhongyuan Lu

Jilin University <https://orcid.org/0000-0001-7884-0091>

Kun Liu

Jilin University <https://orcid.org/0000-0003-2940-9814>

Zhihong Nie (✉ znie@fudan.edu.cn)

Fudan University <https://orcid.org/0000-0001-9639-905X>

Article

Keywords:

Posted Date: August 7th, 2020

DOI: <https://doi.org/10.21203/rs.3.rs-50115/v1>

License:   This work is licensed under a Creative Commons Attribution 4.0 International License.

[Read Full License](#)

Version of Record: A version of this preprint was published at Nature Communications on September 22nd, 2022. See the published version at <https://doi.org/10.1038/s41467-022-33125-y>.

Liquid-crystalline chiral phase formation and structural transitions of dumbbell-shaped colloids

Yang Yang^{1,7}, Guangdong Chen^{1,7}, Hanwen Pei^{2,7}, Xuefei Zhang³, Wei Shi⁴, Mingjie Liu⁴, Charl F. J. Faul⁵, Bai Yang¹, Zhongyuan Lu^{1,2,*}, Kun Liu^{1,6,*} & Zhihong Nie^{3,*}

¹State Key Laboratory of Supramolecular Structure and Materials, College of Chemistry, Jilin University, Changchun 130012, China.

²Institute of Theoretical Chemistry, College of Chemistry, Jilin University, Changchun 130023, China.

³State Key Laboratory of Molecular Engineering of Polymers, Department of Macromolecular Science, Fudan University, Shanghai 200438, China.

⁴Key Laboratory of Bioinspired Smart Interfacial Science and Technology of Ministry of Education, School of Chemistry, Beihang University, Beijing 100191, China.

⁵School of Chemistry, University of Bristol, Bristol BS8 1TS, U.K.

⁶State Key Laboratory of Applied Optics, Changchun Institute of Optics, Fine Mechanics and Physics, Chinese Academy of Sciences, Changchun 130012, China.

⁷These authors contributed equally: Yang Yang, Guangdong Chen, Hanwen Pei.

*Correspondence and requests for materials should be addressed to

Z.L. (email: luzhy@jlu.edu.cn) or to K.L. (email: kliu@jlu.edu.cn) or to Z.N. (email: znie@fudan.edu.cn).

Abstract

Colloidal liquid crystals (LCs) are an emerging class of soft materials that naturally combine the unique properties of both LC molecules and colloidal particles. Chiral LC blue phases are highly attractive in fast optical displays and electrooptical devices, but the formation of chiral structures from achiral colloidal particles is rare. Herein we demonstrate that achiral dumbbell-shaped colloids can assemble into a rich variety of characteristic LC phases, including nematic phases with lock structures, smectic phases, and particularly double-twisted chiral columnar phases. Phase diagrams from experiments and simulations show that the existence and stable regions of different LC phases are strongly dependent on the geometry of colloids. Furthermore, the LC phases can be dynamically tuned by external magnetic fields. This work paves a new route to the development of stimuli-responsive functional LC mesostructures for LC display and laser applications.

Introduction

Liquid crystals (LCs) are a state of matter that bears liquid-like fluidity and crystal-like ordering, which are ubiquitous in the natural world and our everyday life. Chiral LCs possess helical structures arising from the spontaneous twist of LC mesogens. They are intriguing for applications in areas, such as display devices and photonic materials¹. Interestingly enough, chiral LCs can be formed from the chiral organization of achiral objects (e.g., molecules and colloids) that do not have a chiral center²⁻⁶. This phenomenon is of paramount importance from both theoretical and practical perspectives because the synthesis of chiral objects is often difficult and costly. The formation of chiral LCs from achiral building blocks has been predicted by numerous computational researches⁷⁻⁹, however, experimental demonstrations have been rare. Experimental examples of chiral LCs from achiral mesogens have been limited to cholesteric and chiral smectic phases formed by banana-shaped molecules² and their colloidal analogues (i.e., bent-core colloids)³, chiral smectic phase from odd-membered mesogenic dimers⁴, and twist grain boundary phase assembled from graphene⁵. Compared with molecular LCs, colloid-based LC materials are thermally stable, inexpensive, and possess enhanced susceptibility to external fields, including shear fields^{10,11}, electric fields, and magnetic fields¹²⁻¹⁵, which makes them attractive for a wide range of applications such as shearing microlithography¹¹, photonics, and LC displays^{16,17}. Moreover, because of their unique dimensions (from submicrometer to micrometer scale), colloidal particles are ideal model systems for studying LC phase behavior of their molecular counterparts which are difficult to be directly observed and quantitatively studied¹⁸⁻²⁰. Therefore, there is an urgent need to develop new levels of understanding of the chiral formation from achiral colloidal mesogens with novel shapes²¹⁻²⁵.

Dumbbell-shaped colloids (DBC) are featured with distinctive concave geometry and unique packing behavior, making them attractive as building blocks for functional optical materials²⁶⁻²⁸. Nanosized dumbbells with charge patches can pack into zippers, cross-stacks, and open-lattice crystals²⁶. Dumbbell-like nano-arrows can assemble into net-like, zipper-like, and weave-like two-dimensional lattices, as well as non-close-packed three-dimensional supercrystals, depending on the aspect ratio of the colloids²⁷. Moreover, dumbbell-shaped molecules exhibit geometry dependent assembly behavior to produce helical structures²⁹⁻³¹, suggesting the concave geometry can twist the packing of dumbbell-shaped building blocks. Nevertheless, to date, the manner in which the concave geometry of DBCs determines their LC phase behavior has not been explored experimentally, largely due to current challenges in the large-scale synthesis of these colloids with precisely controlled geometries.

This work presents a systematic study of the LC phase behavior of DBCs, which resemble dumbbell-shaped LC mesogens, with precisely tunable geometry^{32,33}. We observe that these DBCs assemble into a rich variety of characteristic LC phases, including double-twisted chiral columnar phase (N^*) with core geometry similar to that of blue phases^{8,9}, nematic phases with one-lock ($N1$) and two-lock ($N2$) structures, and smectic A (SmA) phase (Fig. 1). In particular, the chirality formation in N^* phases from achiral building blocks is of significant interest and has been rarely reported in colloidal systems^{3,5,34}. The equilibrium phases are found to be dictated by the two critical geometric parameters of DBCs, namely, the ratio of diameters (R_D) of end blocks (D_e) to central blocks (D_c), and the ratio of lengths (R_L) of end blocks (L_e) to central blocks (L_c). Brownian dynamic simulations confirm the geometry dependent formation of mesophases and show good agreement with experimental results. The experimental and computational results are summarized in phase diagrams of stable phases and phase transitions in the R_D and R_L space. Moreover, we also demonstrate that the colloidal LC phases can be dynamically manipulated using magnetic fields. This study provides new insights into the phase behavior of dumbbell-shaped objects, and the fabrication of stimuli-responsive functional colloidal materials with desired electronic and photonic properties for LC display and LC laser applications.

Results

LC phases assembled from DBCs with various geometries. DBCs with controlled R_D (1.06–1.77), R_L (0.08–1.81), and L/D_e (1.55–9.93, where L is the overall length of the DBC, i.e., $L = 2L_e + L_c$) were synthesized *via* a wet-chemical method³². The DBCs were dispersed in dimethyl sulfoxide (DMSO) in capillary tubes and left to slowly settle to the bottom (Supplementary Fig. 1)^{13,14}. The LC phases were formed after ~30 days of sedimentation with a volume fraction of ~50%. Notably, similar to molecular LCs, the colloidal LC phases exhibited fluidic behavior and could flow upon tilting the capillary tube (Supplementary Fig. 2). Depending on R_D and R_L , the DBCs assembled into a variety of entropy driven LC mesophases, including N^* , $N2$, $N1$, and SmA phases. The long-range ordering and detailed organization of individual DBCs within all the formed phases were characterized by polarized optical microscopy (POM) and scanning electron microscopy (SEM), respectively.

For DBCs with two very short e-blocks (e.g., $R_L = 0.10$), the colloids organized into the N^* phase with a racemic mixture of double-twisted chiral columns, although the constituent DBCs are achiral (Fig. 2a–c). Within each double-twisted chiral column, the DBCs were rotated in a helical fashion along the long-axis ($\hat{\mathbf{t}}_1$) of each column and also formed a barrel-like chiral twist with respect to its layer normal ($\hat{\mathbf{t}}_2$) (Fig. 1). Statistically, the population of

right- and left-handed chiral columns is approximately equal at a 100 μm length scale. Thus, the N^* phase shows locally defined handedness and helical pitch (\mathbf{P}) that varies slightly from domain to domain. For example, the helical structure in Fig. 2b displays a left-handed column and a right-handed column with a half \mathbf{P} ($1/2\mathbf{P}$) of $\sim 5 \mu\text{m}$. The helical twist can be interrupted when columns with different handedness merge. Within the barrel twist, the central DBC does not tilt with \mathbf{t}_2 , and the tilt angle of DBCs increases from the inner to the outer regime (Fig. 1). The formation of the N^* phase was further confirmed by the characteristic texture in the POM image of periodic lines with a spacing of $\sim 5 \mu\text{m}$, corresponding to $1/2\mathbf{P}$ (Fig. 2c)^{1,5}.

The dumbbell shape endows DBCs with interlocking ability. DBCs with two short e-blocks (e.g., $R_L = 0.56$) assembled into an N_2 phase (Fig. 2d–f). In the nematic phase, the degree of orientational order can be described by the order parameter $S = \frac{1}{2} \langle 3 \cos^2 \theta - 1 \rangle$, where θ is the angle between the director and the long axis of each DBC, and the brackets denote an average over all the measured DBCs³⁵. S varies from 0 (isotropic) to 1 (crystal). As shown in SEM images (Fig. 2d,e), the DBCs show a high degree of long-range orientational order with $S \sim 0.7$. Moreover, neighboring DBCs are packed in a slipped mode to form two-lock structures; that is, the two thick e-blocks of two end-to-end adjacent DBCs are embedded within the groove (i.e., thin c-block) of a third DBC. The localized POM image (Fig. 2f) shows the typical schlieren texture of the N_2 LC phase. DBCs with two intermediate e-blocks (e.g., $R_L = 0.99$) organized into the N_1 phase (Fig. 2g–i). The detailed packing of DBCs is shown in Fig. 2g,h. The concavity of one DBC does not have sufficient room to accommodate two e-blocks of neighboring DBCs to form the two-lock structure. Instead, the groove of each DBC fits one e-block of an adjacent DBC to form the one-lock structure with $S \sim 0.8$. The N_1 phase also exhibits a schlieren texture (Fig. 2i). DBCs with two long e-blocks (e.g., $R_L = 1.29$) exhibited a SmA phase with the average rod alignment perpendicular to the smectic layer (Fig. 2j–l). The individual DBCs are located within the smectic layer (as shown in Fig. 2j,k). The formation of the SmA phase was also confirmed by the characteristic striped texture in the POM image (Fig. 2l).

Phase diagram and geometric effects based on experimental observations. The assembled phases of DBCs were mapped out in a phase diagram in the space of R_D and R_L (Fig. 3a). The achiral DBCs with two very short e-blocks ($R_D > 1.1$ and $R_L < 0.45$) underwent spontaneous chiral symmetry breaking, leading to the N^* phase with chiral superstructures (Supplementary Fig. 3). Due to the DBCs' strong tendency to align with each other and the adjacent DBCs not being confined to a planar surface, the steric hindrance between adjacent DBCs induces twists,

which eventually generates chiral assembled structures³⁶. DBCs can twist in two equivalent ways (Fig. 1), thus leading to the formation of racemic mixtures with equal probability of right- and left-handed chiral domains. It is found that \mathbf{P} is strongly dependent on the value of L_c/D_e (Fig. 3b). \mathbf{P} increases from 7 to 17 μm with L_c/D_e increasing from 3.0 to 8.5. To the best of our knowledge, this is the first experimental demonstration of the formation of a double-twisted LC phase from achiral DBCs. This phenomenon is in agreement with previous simulation studies on polymer-tethered nanorods⁷, bent-core, and linear rigid particles^{8,9}.

As R_L increases, DBCs with two short e-blocks ($1.3 < R_D < 1.6$ and $R_L \sim 0.50$) form the N2 phase, as DBCs with two-lock arrangements can pack more efficiently than the simple nematic phase (Supplementary Fig. 4). With the further increase of R_L , L_e becomes comparable to L_c . The shape complementarity in the morphology leads to the N1 phase with zipper structures (Supplementary Fig. 5)²⁶ for DBCs with two intermediate e-blocks ($1.1 < R_D < 1.6$ and $R_L \sim 1.00$). Notably, the dashed lines at R_L of 0.50 and 1.00 locate around the centers of N2 and N1 phases, respectively. For DBCs with long e-blocks ($R_L > 1.35$) or DBCs with small diameter differences ($R_D < 1.1$), SmA phases are formed due to the mismatch between L_e and L_c of DBCs and the nearly rod-like shape of DBCs (Supplementary Fig. 6)³⁷. For DBCs with large diameter difference ($R_D > 1.6$), isotropic phases (i.e., without orientational and positional order) were found (Supplementary Fig. 7). The formation of the isotropic phase can be attributed to the large energy barriers for the assembly of DBCs. In summary, these results indicate that subtle variation in the geometry of DBCs has a significant impact on their phase behavior.

Simulations based on a coarse-grained Brownian dynamics model. We simulated the LC phase formation of DBCs with different geometric parameters using a coarse-grained Brownian dynamics model (see Methods for simulation details)³⁸. Briefly, the DBCs were constructed by freezing linearly arranged rigid spherical beads into a dumbbell rod geometry in accordance with the size and shape of real DBCs. The e-blocks with a large diameter D_e were located at both ends of the central c-block with a small diameter D_c . The interactions between DBCs were set to be purely repulsive Weeks-Chandler-Andersen (WCA) potential³⁹. All simulations were carried out in a cubic cell with periodic boundary conditions. To simulate the phase condition with high densities, the length of box size was iteratively increased and decreased upon changing the temperature.

The formation of all the phases observed in the experiments was confirmed by the simulations. Figure 4 shows four characteristic snapshots of the assembled DBCs with different values for R_D and R_L . The simulation results indicate that the assembled phases of DBCs are strongly dependent on R_L , which is consistent with the

experimental results. When R_D was fixed as 1.40, the DBCs with $R_L = 0.15$ accommodated in an N^* phase. Figure 4a,e show the configuration of a single column extracted from the simulation box. The snapshots clearly show that, rather than packing parallel to each other, the DBCs form a regular chiral twist both within and about the column. In this case, the e-blocks prevent regular close packing of the DBCs, which would otherwise lead to the formation of the smectic phase. As a result, the neighboring DBCs are closely packed with a tilted angle to form the twisted structure. It should be noted that these assembled structures exhibit a discontinuity in the twist of the column because of the convergence of columns with different handedness. DBCs with $R_L = 0.50$ form an N_2 phase (Fig. 4b). Typically, two e-blocks of two end-to-end adjacent DBCs are trapped in one concave groove of an adjacent DBC. In the local structure of the N_2 phase, a total of six DBCs (three green e-blocks above and three blue e-blocks below) packed around the central red c-block. In other words, two layers of e-blocks from surrounding rods are trapped by the central c-block along its long axis. In contrast, DBCs with $R_L = 1.00$ exhibit an N_1 phase (Fig. 4c). One e-block of each DBC is preferentially embedded in the concave groove of an adjacent DBC. This configuration allows DBCs to pack closely with neighboring ones, resulting in a zipper structure. As R_L increases, DBCs with $R_L = 1.80$ become stable in the SmA phase (Fig. 4d). In this case, since the e-block is longer than the c-block, the e-block cannot be fit into the concave groove of a DBC. Therefore, the effect of the diameter difference of blocks becomes negligible, making them behave like conventional colloidal rods³⁷. Finally, it was found that only DBCs with $1.1 \leq R_D < 1.6$ could exhibit assembly behavior that are distinct from rod-like colloids. DBCs with even larger R_D (≥ 1.6) tend to form an isotropic phase (i.e., without positional and orientational order) due to the high energy required for the assembly of DBCs (Supplementary Fig. 8).

Phase diagram and geometric effects based on simulations. We evaluated the formation and transitions of mesophases by systematically varying R_D and R_L in simulations. The results are summarized in the phase diagram shown in Fig. 5. The phase regions are in good agreement with the experimental phase diagram. The formation of mesophases is determined by both R_D and R_L . The N^* phase is stable only when R_L is small, i.e., the DBCs possess two very short e-blocks (Supplementary Fig. 9). Chirality of the structure arises from the twist arrangement of achiral DBCs. When the e-block becomes longer the formation of the N^* phase is suppressed, while the formation of N_2 and N_1 phases is strongly promoted. The N_2 phase is formed when R_L is around 0.5 (i.e., the length of c-block is approximately twice of that of e-block). In this case, the concave groove of a DBC can accommodate two e-blocks in the long axis direction, which is driven by excluded volume interactions (Supplementary Fig. 10). The N_1 phase

was observed with further increasing R_L to about 1.0. The comparable length of c-block to e-block enables the trapping of one e-block in each concave groove of DBCs in the long axis direction. When the e-block is longer than the c-block, the DBCs form the SmA phase.

LC Phase manipulation with magnetic fields. Thanks to the positive diamagnetic anisotropy of DBCs, the colloidal LCs of DBCs are responsive to external magnetic fields, and the LC phases can be dynamically tuned by controlling the DBC orientation. Upon applying a magnetic field of 5 T, DBCs were rotated and aligned their long axis along the field direction, resulting in their visual texture changing from N^* to regular nematic phase as shown in the POM images (Supplementary Fig. 11). The strip pattern of nematic phase is well-aligned to the magnetic field. In addition, fewer defects were observed after the application of the magnetic field, indicating the efficient alignment of DBCs by the magnetic field. This result suggests the potential of such DBC-based colloidal phases for application in stimuli-responsive and magnetically switchable systems.

Discussion

In conclusion, we have systematically studied the phase behavior of the colloidal analogues of dumbbell-shaped molecules, so-called dumbbell-shaped colloids (DBC). We demonstrated, using both experimental and simulation data, the critical role of colloidal geometry in the formation of mesoscopically ordered phases. Our experimental results showed that DBCs with R_D ranging from 1.0 to 1.8 and R_L ranging from 0.1 to 1.8 assembled into a variety of LC phases including N^* , N_2 , N_1 , and SmA phases. The phases and onset of phase transitions were found to be strongly dependent on the geometric parameters (i.e., R_D and R_L) of the DBCs. It is worth noting that double-twisted chiral superstructures with racemic mixtures can be produced from rigid achiral colloids. Brownian dynamics simulation was used to further establish the correlation between the geometry and phase formation of DBCs. The simulation results are in good agreement with the experimental data, providing a theoretical basis for the future design of complex mesogenic systems. In addition, we show that the colloidal LC phases can be dynamically tuned by controlling the orientation of DBCs with magnetic fields. This work provides new insight into the rules required for the design of particles of different shapes to achieve superstructures with increased complexity and desired stimuli-responsive electronic and photonic properties.

Methods

Synthesis of DBCs. DBCs were synthesized by a recently developed emulsion-templated wet-chemical approach³². In a typical experiment, 500 mg polyvinylpyrrolidone ($M_w = 40,000$, Sigma-Aldrich) was dissolved in 5.0 ml 1-pentanol (99%, Sigma-Aldrich) in a 10 ml glass vial under sonication. 140 μ l deionized water (18.2 M Ω), 50 μ l 0.18 M sodium citrate dihydrate (99%, Sigma-Aldrich) aqueous solution, 475 μ l anhydrous ethanol (Pharmco-Aaper), and 100 μ l ammonium hydroxide solution (28 wt%, Sigma-Aldrich) were added to the glass vial and vortexed for 1 min. After the mixture was left standing for 5 min to release gas bubbles, 50 μ l tetraethylorthosilicate (TEOS, 98%, Sigma-Aldrich) was added and the solution was then gently shaken for 30 s. The L_e (160–900 nm) and L_c (170–3360 nm) of DBCs can be individually controlled by tuning the reaction time during the growth of each block. The D_e of DBCs can be tuned from 190 to 460 nm by adjusting the amount of ammonium hydroxide. The D_c of DBCs can be adjusted in the range of 140–340 nm by varying the strength of perturbation in the reaction temperature (25–70 °C) during the DBC growth. A higher temperature during the perturbation period produces a smaller D_c . For example, for DBCs with $L_e = 160$ nm, $L_c = 1660$ nm, $D_e = 315$ nm, and $D_c = 240$ nm, the reaction mixture was incubated at 25 °C for 30 min, 60 °C for 20 min, and 25 °C for another 4 h.

Purification. The as-synthesized DBCs were purified by centrifugation at 6000 rpm for 10 min. The precipitated DBCs were then washed three times with ethanol under centrifugation at 3000 rpm. Finally, the DBCs were suspended in ethanol and centrifuged at 1000 rpm for 10 min to remove small particles and other lightweight impurities.

Assembly of DBCs into LCs. The DBC dispersions in DMSO (99.9%, Fisher Chemical) with a volume fraction of 20% were filled into one-end-sealed glass capillaries (Stuart) with an outside diameter of 1.9 mm, an inside diameter of 1.3 mm, and a length of 100 mm, and rectangular capillaries (VitroCom) with 2.0 mm in width, 0.2 mm in inner-thickness, 0.14 mm in wall thickness, and 50 mm in length. The other ends of the capillaries were then sealed by melting. Subsequently, the capillaries were left in a vertical position for the sedimentation of DBCs. After one month, the capillaries were opened, and the sediment was taken out and slowly dried in air at room temperature for SEM characterizations. The samples in rectangular capillaries were directly used for POM characterization.

Phase switching with magnetic fields. The switching of colloidal LC phases was conducted under a magnetic field generated by 9 T Room Temperature Bore Magnet System (Cryomagnetics, Inc). The samples in rectangular

capillaries upon sedimentation were allowed to sit undisturbed for 1 hour under a magnetic field of 5 T and then examined using POM.

Characterizations. The SEM images of DBCs and their assemblies were taken using a Hitachi SU-70 Schottky field emission gun SEM at an operation voltage of 10 kV. POM images were obtained by an Olympus BX50F4 Microscope with crossed polarizing filters.

Computer simulations. Computer simulations on the formation mechanism of different structures of DBCs were approached as follow: the e-block and c-block with the diameters of D_e and D_c were constructed by freezing linearly arranged spherical beads, respectively. Two e-blocks with a diameter of D_e were located at both ends of a DBC. Each DBC was treated as a rigid body in the simulation. Non-bonding interactions between DBCs were described by the WCA potential. The WCA potential is the 12-6 Lennard-Jones potential truncated at the energy minimum and shifted vertically by $\epsilon/k_B T$; it is a purely repulsive potential featuring the volume occupied by DBCs. The Brownian dynamics of rigid bodies in the canonical ensemble was adopted for the simulations. The details of the simulation method can be found in Ref. 38. The length and the energy units of the simulation system are σ and ϵ , respectively. The time step is in a unit of $\sigma\sqrt{m/T}$, while the unit of temperature is ϵ/k_B . A leapfrog algorithm of rigid bodies with a time step of $\Delta t = 0.01$ was adopted to integrate the equations of motion⁴⁰.

In the simulations, DBCs in the initial configuration were regularly generated in the simulation box with a volume fraction of 0.48. The regular initial configuration is helpful for testing whether the smectic structure is stable under certain simulation conditions and getting the physical insight of the formation mechanism of different structures. Then the temperature of the system was iteratively increased and decreased between $0.5k_B/\epsilon$ and $1.0k_B/\epsilon$ with an interval of $\Delta T = 0.05k_B/\epsilon$ every 2×10^6 timesteps. The box size in z-direction was also iteratively increased and decreased with the variance of temperature. The volume fraction was varied between 0.46 and 0.48. Finally, the system was further equilibrated for 1×10^7 timesteps at the 0.48 volume fraction⁴¹. In the present work, the parameter L/D_e was fixed at around 5 except for some special cases. This value corresponds to a moderate rod length according to our previous work³. The values of L/D_e in several systems with extremely small R_L (i.e., 0.08, 0.12 and 0.15) were set as 11.5, 7.0 and 8.1, respectively.

Data availability. The authors declare that the data supporting the findings of this study are available within the article and its Supplementary Information files.

References

1. Shopsowitz, K. E., Qi, H., Hamad, W. Y. & MacLachlan, M. J. Free-standing mesoporous silica films with tunable chiral nematic structures. *Nature* **468**, 422-425, (2010).
2. Link, D. R. *et al.* Spontaneous Formation of Macroscopic Chiral Domains in a Fluid Smectic Phase of Achiral Molecules. *Science* **278**, 1924-1927, (1997).
3. Yang, Y. *et al.* Phase behaviors of colloidal analogs of bent-core liquid crystals. *Science Advances* **4**, eaas8829, (2018).
4. Abberley, J. P. *et al.* Heliconical smectic phases formed by achiral molecules. *Nat. Commun.* **9**, 228, (2018).
5. Xu, Z. & Gao, C. Graphene chiral liquid crystals and macroscopic assembled fibres. *Nat. Commun.* **2**, 571, (2011).
6. Gibaud, T. *et al.* Reconfigurable self-assembly through chiral control of interfacial tension. *Nature* **481**, 348, (2012).
7. Horsch, M. A., Zhang, Z. & Glotzer, S. C. Self-Assembly of Polymer-Tethered Nanorods. *Phys. Rev. Lett.* **95**, 056105, (2005).
8. Yan, F., Hixson, C. A. & Earl, D. J. Self-Assembled Chiral Superstructures Composed of Rigid Achiral Molecules and Molecular Scale Chiral Induction by Dopants. *Phys. Rev. Lett.* **101**, 157801, (2008).
9. Yan, F., Hixson, C. A. & Earl, D. J. Computer simulations of linear rigid particles that form chiral superstructures and tilted smectic phases. *Soft Matter* **5**, 4477-4483, (2009).

10. Alizadehgiashi, M. *et al.* Shear-Induced Alignment of Anisotropic Nanoparticles in a Single-Droplet Oscillatory Microfluidic Platform. *Langmuir* **34**, 322-330, (2018).
11. Jiang, Y., Guo, F., Xu, Z., Gao, W. & Gao, C. Artificial colloidal liquid metacrystals by shearing microlithography. *Nat. Commun.* **10**, 4111, (2019).
12. van der Kooij, F. M., Kassapidou, K. & Lekkerkerker, H. N. W. Liquid crystal phase transitions in suspensions of polydisperse plate-like particles. *Nature* **406**, 868-871, (2000).
13. Marechal, M., Kortschot, R. J., Demirörs, A. F., Imhof, A. & Dijkstra, M. Phase Behavior and Structure of a New Colloidal Model System of Bowl-Shaped Particles. *Nano Lett.* **10**, 1907-1911, (2010).
14. Kuijk, A., van Blaaderen, A. & Imhof, A. Synthesis of Monodisperse, Rodlike Silica Colloids with Tunable Aspect Ratio. *J. Am. Chem. Soc.* **133**, 2346-2349, (2011).
15. Yang, Y. *et al.* Synthesis and assembly of colloidal cuboids with tunable shape biaxiality. *Nat. Commun.* **9**, 4513, (2018).
16. Sang Ouk Kim, Ji Eun Kim, Tae Hee Han, Sun Hwa Lee, Ju Young Kim. Graphene composition having liquid crystalline properties and preparation method thereof [P]. US 8449791 B2, 2013-05-28.
17. Vesna Müller, Heiko Briesen. Nanocrystalline cellulose, its preparation and uses of such nanocrystalline cellulose [P]. EP 3006468 A1, 2016-03-14.
18. Li, F., Josephson, D. P. & Stein, A. Colloidal Assembly: The Road from Particles to Colloidal Molecules and Crystals. *Angew. Chem., Int. Ed.* **50**, 360-388, (2011).
19. Chen, Q., Bae, S. C. & Granick, S. Directed self-assembly of a colloidal kagome lattice. *Nature* **469**, 381, (2011).
20. Manoharan, V. N. Colloidal matter: Packing, geometry, and entropy. *Science* **349**, (2015).
21. Glotzer, S. C. & Solomon, M. J. Anisotropy of building blocks and their assembly into complex structures. *Nat. Mater.* **6**, 557-562, (2007).

22. Henzie, J., Grünwald, M., Widmer-Cooper, A., Geissler, P. L. & Yang, P. Self-assembly of uniform polyhedral silver nanocrystals into densest packings and exotic superlattices. *Nat. Mater.* **11**, 131-137, (2012).
23. Damasceno, P. F., Engel, M. & Glotzer, S. C. Predictive Self-Assembly of Polyhedra into Complex Structures. *Science* **337**, 453-457, (2012).
24. Li, B., Zhou, D. & Han, Y. Assembly and phase transitions of colloidal crystals. *Nat. Rev. Mater.* **1**, 15011, (2016).
25. Boles, M. A., Engel, M. & Talapin, D. V. Self-Assembly of Colloidal Nanocrystals: From Intricate Structures to Functional Materials. *Chem. Rev.* **116**, 11220-11289, (2016).
26. Walker, D. A., Leitsch, E. K., Nap, R. J., Szleifer, I. & Grzybowski, B. A. Geometric curvature controls the chemical patchiness and self-assembly of nanoparticles. *Nat. Nanotechnol.* **8**, 676, (2013).
27. Wang, Q. *et al.* Controlled growth and shape-directed self-assembly of gold nanoarrows. *Science Advances* **3**, e1701183, (2017).
28. Hosein, I. D., Ghebrebrhan, M., Joannopoulos, J. D. & Liddell, C. M. Dimer Shape Anisotropy: A Nonspherical Colloidal Approach to Omnidirectional Photonic Band Gaps. *Langmuir* **26**, 2151-2159, (2010).
29. Köhler, K. *et al.* Self-Assembly in a Bipolar Phosphocholine–Water System: The Formation of Nanofibers and Hydrogels. *Angew. Chem., Int. Ed.* **43**, 245-247, (2004).
30. Bae, J. *et al.* Helical Nanofibers from Aqueous Self-Assembly of an Oligo(p-phenylene)-Based Molecular Dumbbell. *J. Am. Chem. Soc.* **127**, 9668-9669, (2005).
31. Meister, A. *et al.* Helical Nanofibers of Self-Assembled Bipolar Phospholipids as Template for Gold Nanoparticles. *The Journal of Physical Chemistry B* **112**, 4506-4511, (2008).
32. Datskos, P. & Sharma, J. Synthesis of Segmented Silica Rods by Regulation of the Growth Temperature. *Angew. Chem., Int. Ed.* **53**, 451-454, (2014).

33. Lee, M., Jeong, Y.-S., Cho, B.-K., Oh, N.-K. & Zin, W.-C. Self-Assembly of Molecular Dumbbells into Organized Bundles with Tunable Size. *Chem. Eur. J.* **8**, 876-883, (2002).
34. Donkai, N., Hoshino, H., Kajiwara, K. & Miyamoto, T. Lyotropic mesophase of imogolite, 3 observation of liquid crystal structure by scanning electron and noval polarized optical microscopy. *Makromol. Chem.* **194**, 559-580, (1993).
35. Kityk, A. V. *et al.* Thermotropic orientational order of discotic liquid crystals in nanochannels: an optical polarimetry study and a Landau–de Gennes analysis. *Soft Matter* **10**, 4522-4534, (2014).
36. Zerrouki, D., Baudry, J., Pine, D., Chaikin, P. & Bibette, J. Chiral colloidal clusters. *Nature* **455**, 380, (2008).
37. Kuijk, A., Byelov, D. V., Petukhov, A. V., van Blaaderen, A. & Imhof, A. Phase behavior of colloidal silica rods. *Faraday Discuss.* **159**, 181-199, (2012).
38. Zhang, Horsch, M. A., Lamm, M. H. & Glotzer, S. C. Tethered Nano Building Blocks: Toward a Conceptual Framework for Nanoparticle Self-Assembly. *Nano Lett.* **3**, 1341-1346, (2003).
39. Xu, J., Selinger, R. L. B., Selinger, J. V. & Shashidhar, R. Monte Carlo simulation of liquid-crystal alignment and chiral symmetry-breaking. *J. Chem. Phys.* **115**, 4333-4338, (2001).
40. Nguyen, T. D., Jankowski, E. & Glotzer, S. C. Self-Assembly and Reconfigurability of Shape-Shifting Particles. *ACS Nano* **5**, 8892-8903, (2011).
41. Xu, J., Selinger, R. L. B., Selinger, J. V., Ratna, B. R. & Shashidhar, R. Monte Carlo simulation of smectic liquid crystals and the electroclinic effect: The role of molecular shape. *Phy. Rev. E* **60**, 5584-5590, (1999).

Acknowledgments

We acknowledge the support of the State Key Laboratory of Supramolecular Structure and Materials, and the State Key Laboratory of Molecular Engineering of Polymers. We thank the National Natural Science Foundation of China (51973038, 21534004, 91963107, 21674042, and 21911530179), the National Key R&D Program of China (2018YFB0703701), and the Program for JLU Science and Technology Innovative Research Team (JLUSTIRT2017TD-06) for financial support.

Author contributions

Y.Y., Z.L., K.L., and Z.N. designed research. Y.Y. and G.C. performed experiments. H.P. performed simulations. Y.Y., G.C., H.P., X.Z., W.S., Z.L., K.L., and Z.N. analyzed data. M.L., C.F., and B.Y. provided valuable suggestions for the discussion of the results. Y.Y., Z.L., K.L., and Z.N. prepared the manuscript. All the authors read and commented on the manuscript.

Additional information

Competing financial interests: The authors declare no competing financial interests.

Figure legends

Figure 1 | Schematic illustration of four typical LC phases assembled from DBCs. Schematic illustrations of the geometric parameters of DBCs and the corresponding assembled N*, N2, N1, and SmA phases.

Figure 2 | LC phases of DBCs with different geometries. Representative low (a,d,g,j) and high (b,e,h,k) magnification SEM images, and (c,f,i,l) POM images of LC phases assembled from different DBCs: (a,b,c) N* phase assembled from DBCs with $L_e = 160$ nm, $L_c = 1660$ nm, $D_e = 315$ nm, and $D_c = 240$ nm, (d,e,f) N2 phase assembled from DBCs with $L_e = 400$ nm, $L_c = 715$ nm, $D_e = 280$ nm, and $D_c = 190$ nm, (g,h,i) N1 phase assembled from DBCs with $L_e = 515$ nm, $L_c = 520$ nm, $D_e = 235$ nm, and $D_c = 155$ nm, (j,k,l) SmA phase assembled from DBCs with $L_e = 900$ nm, $L_c = 700$ nm, $D_e = 245$ nm, and $D_c = 225$ nm.

Figure 3 | Correlation between geometry and LC phases of DBCs based on experimental results. (a) Experimental phase diagram of DBCs as a function of R_D and R_L . The solid symbols represent the data points in Fig. 2. The black dashed lines indicate superficial boundaries between phases. The red lines correspond to $R_L = 0.5$ and $R_L = 1.0$, respectively. They locate approximately at the center of the corresponding phases, namely N2 and N1 phases. (b) Helical pitch P as a function of L_c/D_e .

Figure 4 | LC phases observed in Brownian dynamics simulations. Simulation results of LC phases assembled from DBCs with (a) $R_D = 1.40$ and $R_L = 0.15$ in N* phase (right: a double-twisted column extracted from left), (b) $R_D = 1.40$ and $R_L = 0.50$ in N2 phase (right: side and bottom view of the typical local structure), (c) $R_D = 1.40$ and $R_L = 1.00$ in N1 phase (right: a cylinder picked out along the z-axis), and (d) $R_D = 1.40$ and $R_L = 1.80$ in the SmA phase (right: a cylinder picked out along the z-axis). (e) Double-twisted structure viewed from different directions.

Figure 5 | Phase diagram based on simulation results. Computational phase diagram of DBCs as a function of R_D and R_L . The boundary dashed lines are taken from the experimental phase diagram.

Figure 1.

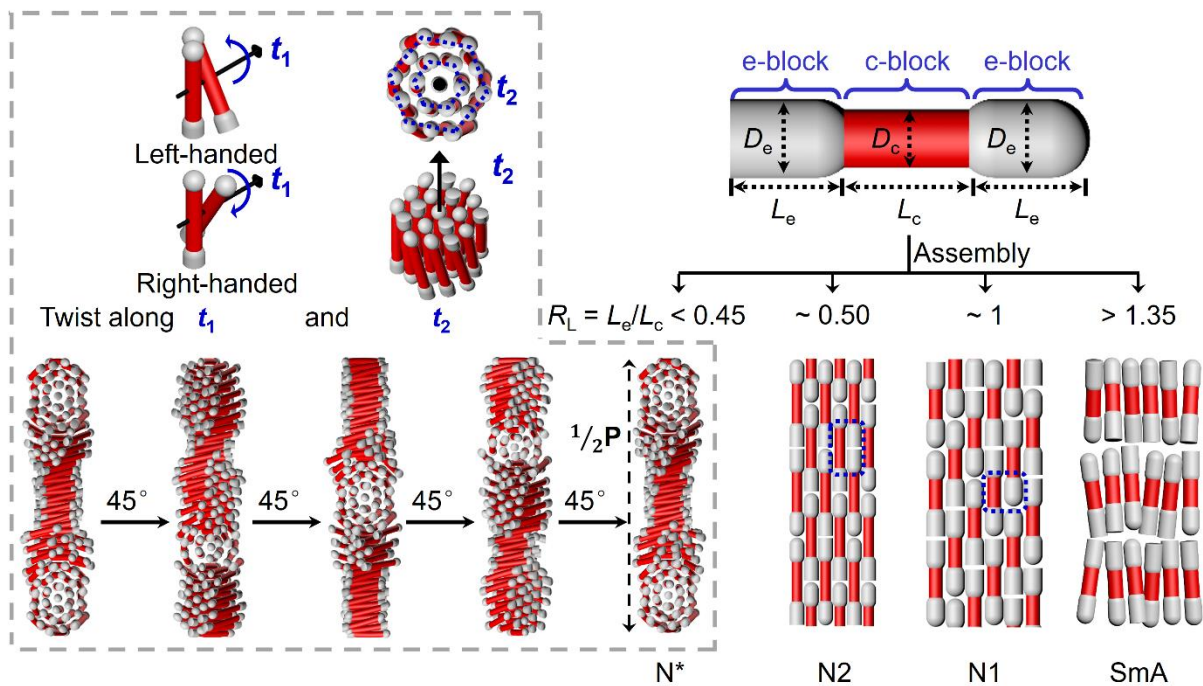


Figure 2.

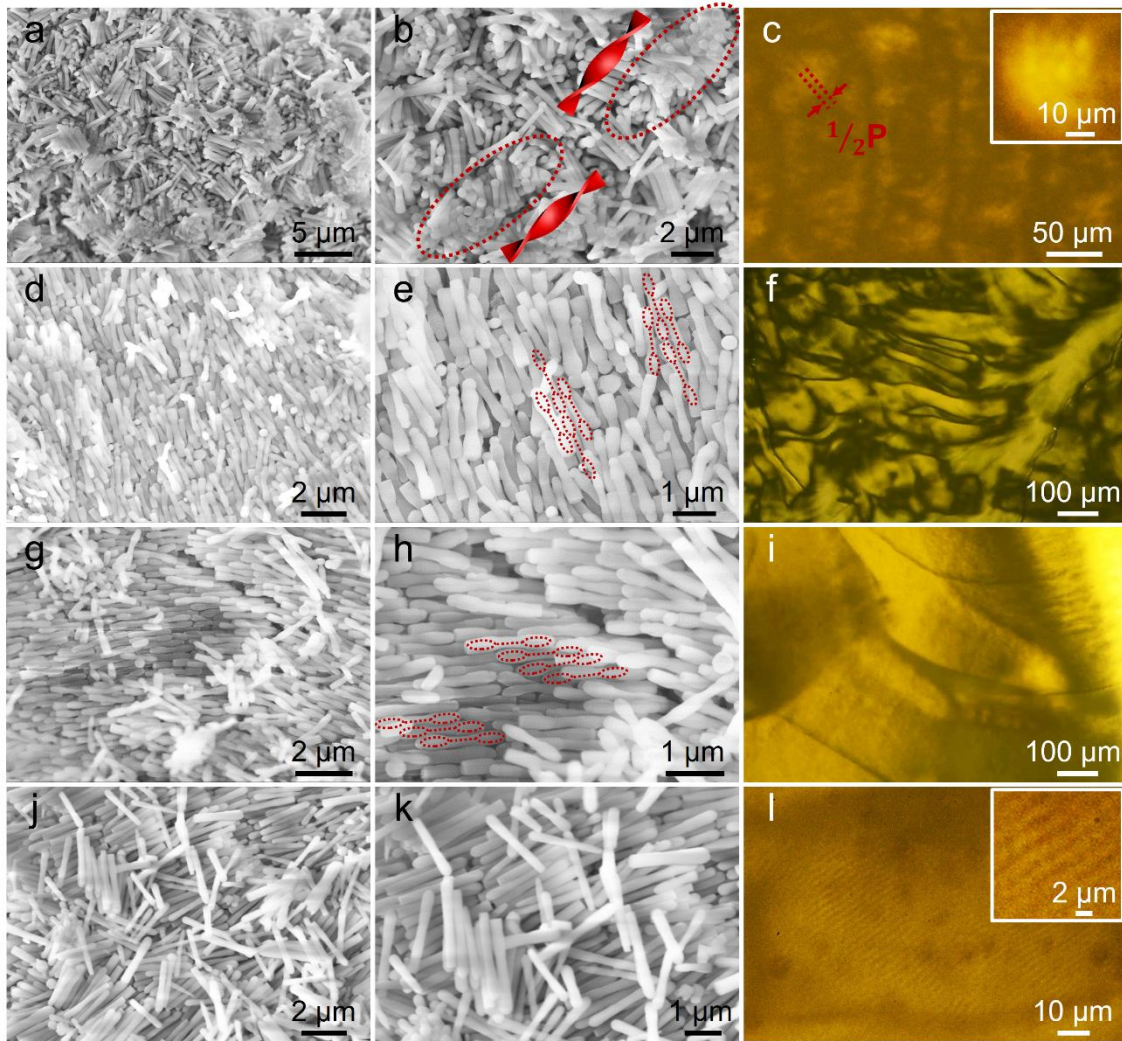


Figure 3.

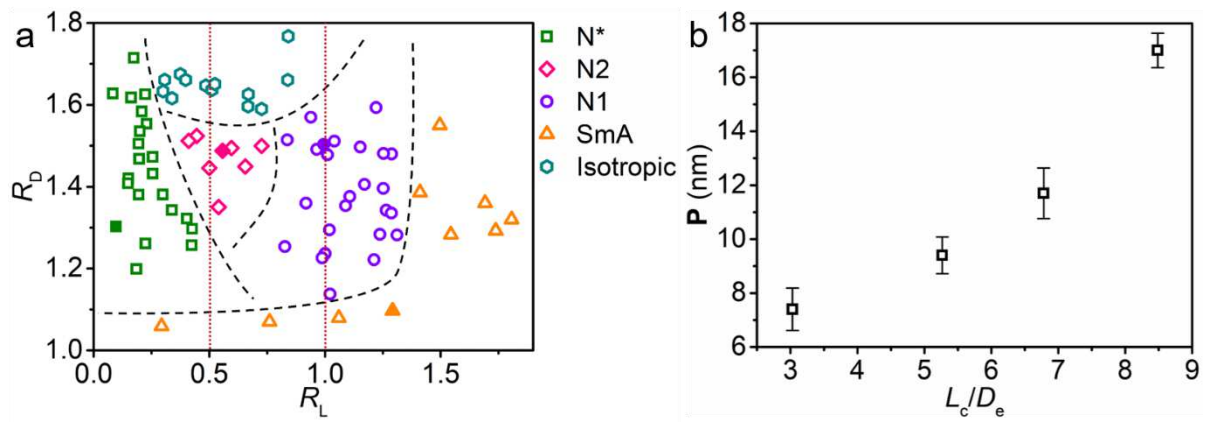


Figure 4.

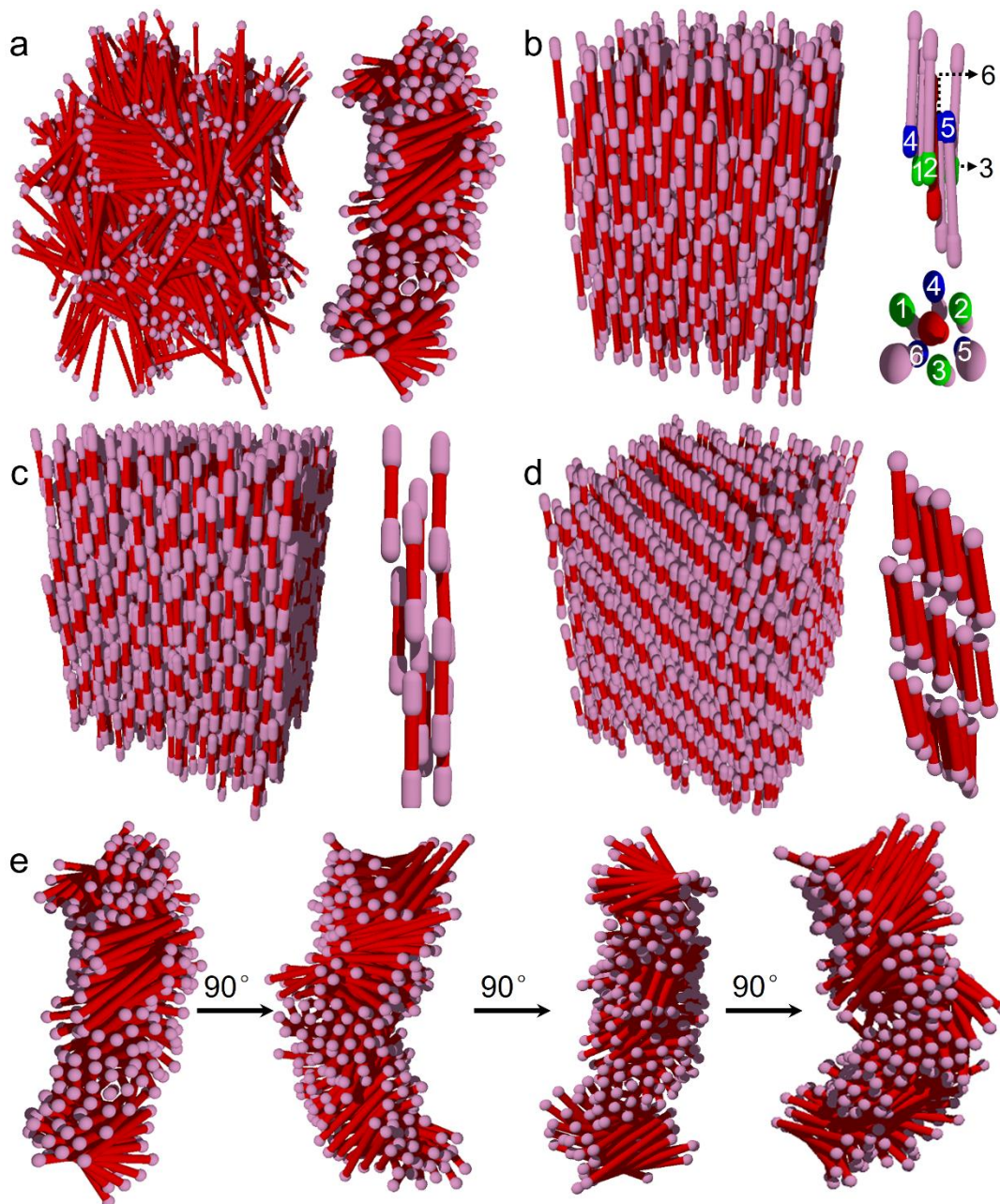
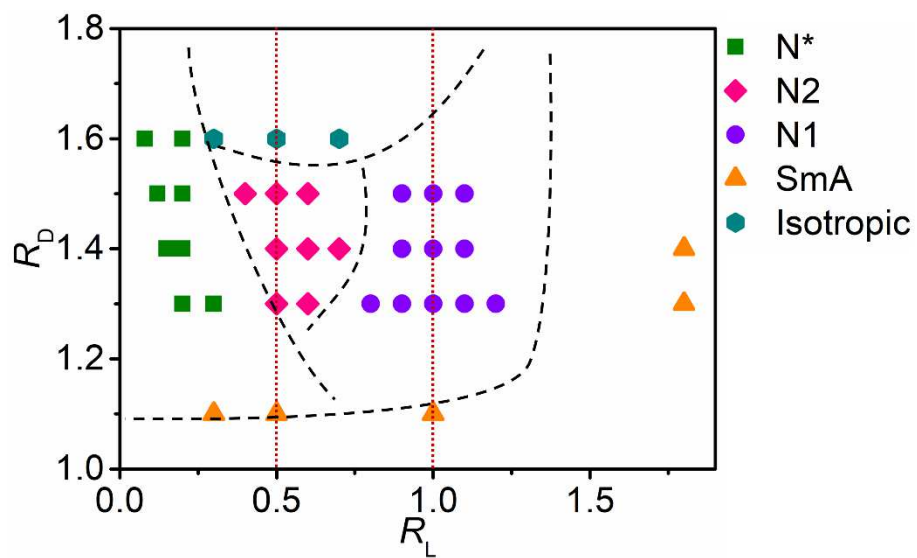


Figure 5.



Figures

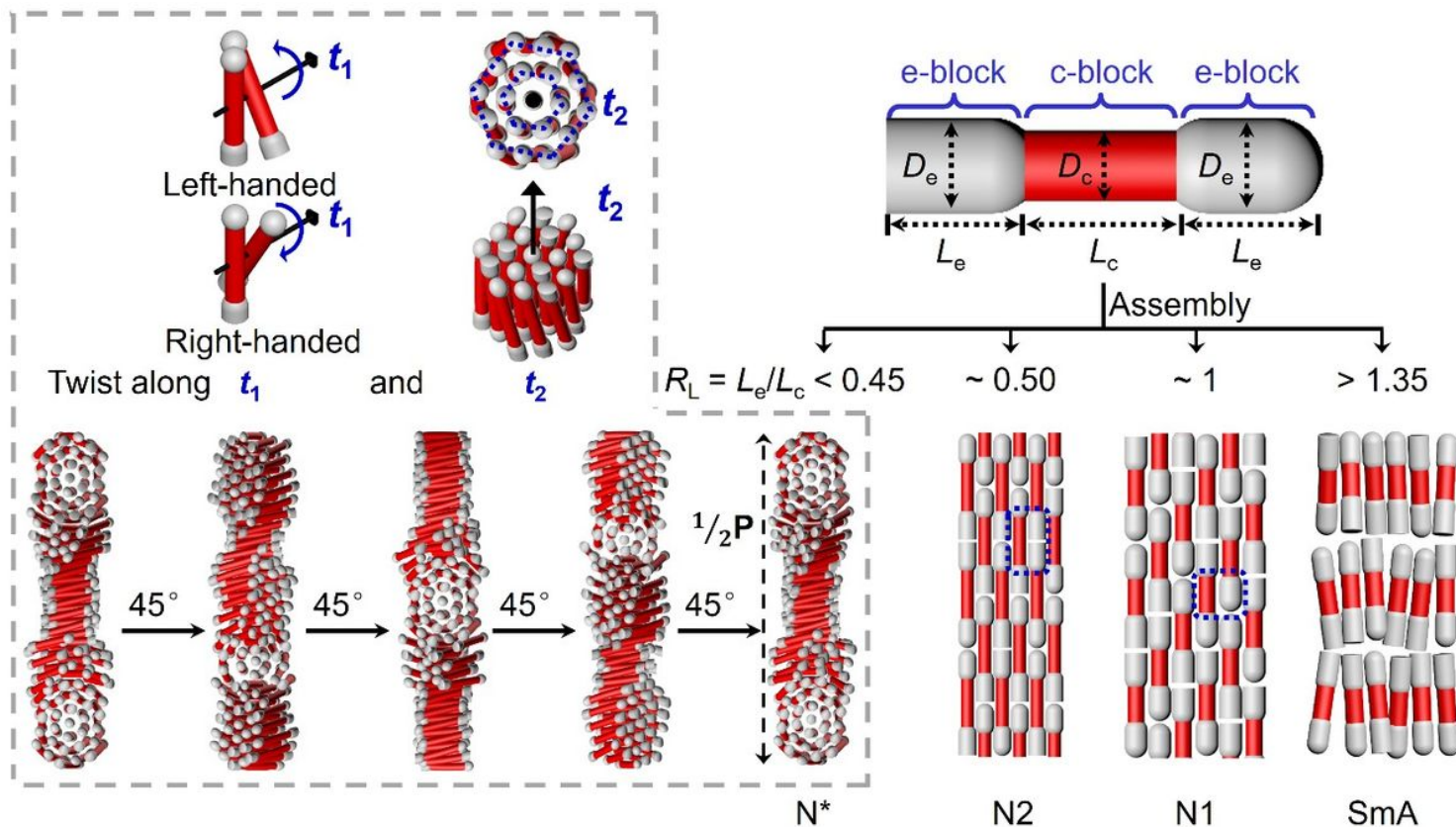


Figure 1

Schematic illustration of four typical LC phases assembled from DBCs. Schematic illustrations of the geometric parameters of DBCs and the corresponding assembled N^* , $N2$, $N1$, and SmA phases.

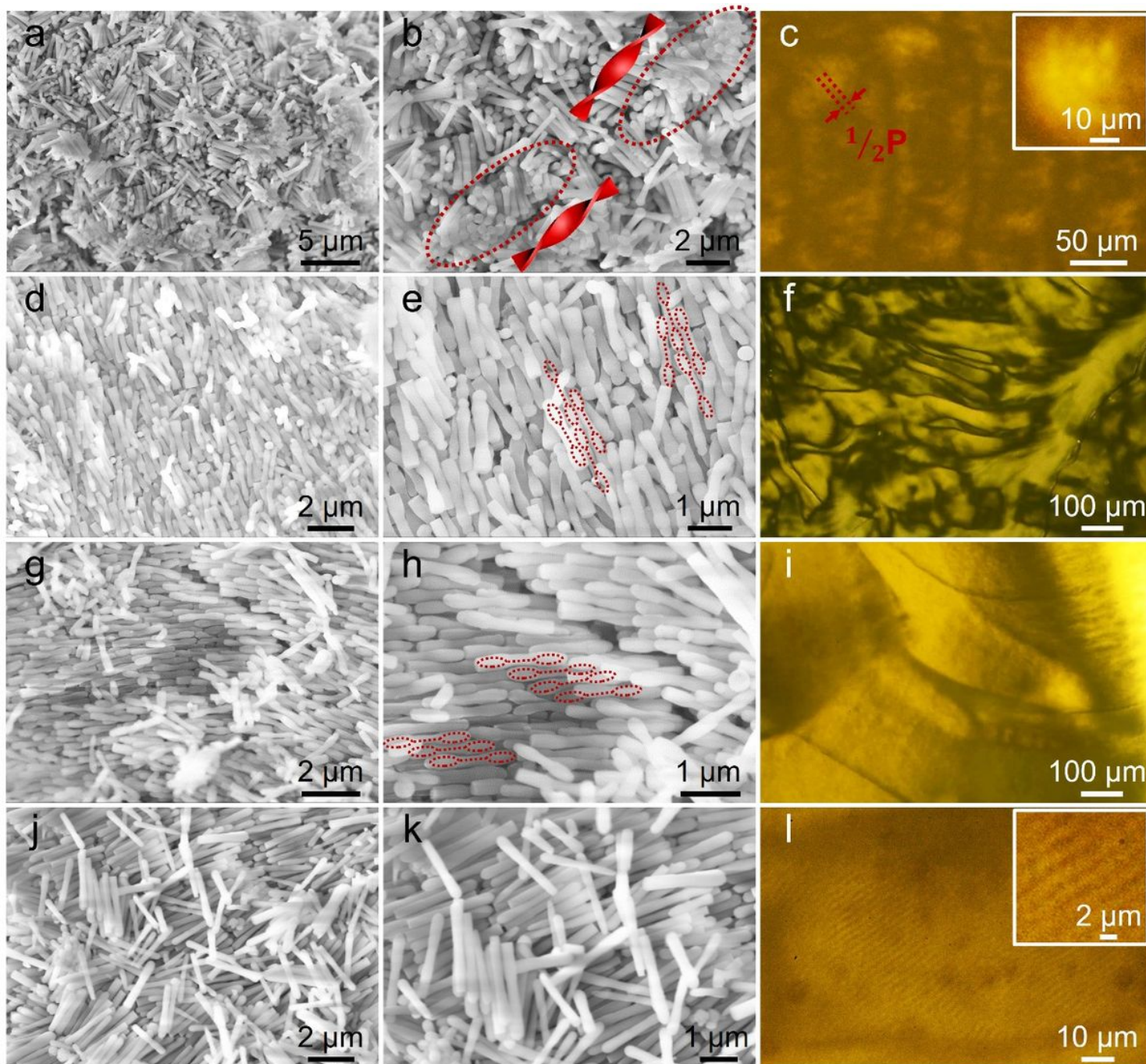


Figure 2

LC phases of DBCs with different geometries. Representative low (a,d,g,j) and high (b,e,h,k) magnification SEM images, and (c,f,i,l) POM images of LC phases assembled from different DBCs: (a,b,c) N* phase assembled from DBCs with $L_e = 160$ nm, $L_c = 1660$ nm, $D_e = 315$ nm, and $D_c = 240$ nm, (d,e,f) N2 phase assembled from DBCs with $L_e = 400$ nm, $L_c = 715$ nm, $D_e = 280$ nm, and $D_c = 190$ nm, (g,h,i) N1 phase assembled from DBCs with $L_e = 515$ nm, $L_c = 520$ nm, $D_e = 235$ nm, and $D_c = 155$ nm, (j,k,l) SmA phase assembled from DBCs with $L_e = 900$ nm, $L_c = 700$ nm, $D_e = 245$ nm, and $D_c = 225$ nm.

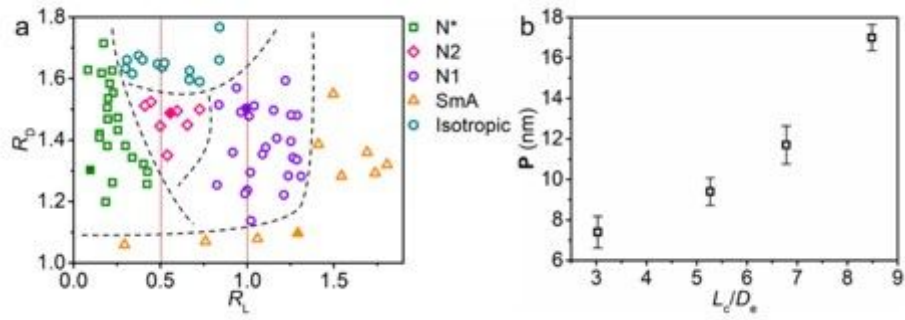


Figure 3

Correlation between geometry and LC phases of DBCs based on experimental results. (a) Experimental phase diagram of DBCs as a function of R_D and R_L . The solid symbols represent the data points in Fig. 2. The black dashed lines indicate superficial boundaries between phases. The red lines correspond to $R_L = 0.5$ and $R_L = 1.0$, respectively. They locate approximately at the center of the corresponding phases, namely N2 and N1 phases. (b) Helical pitch P as a function of L_c/D_e .

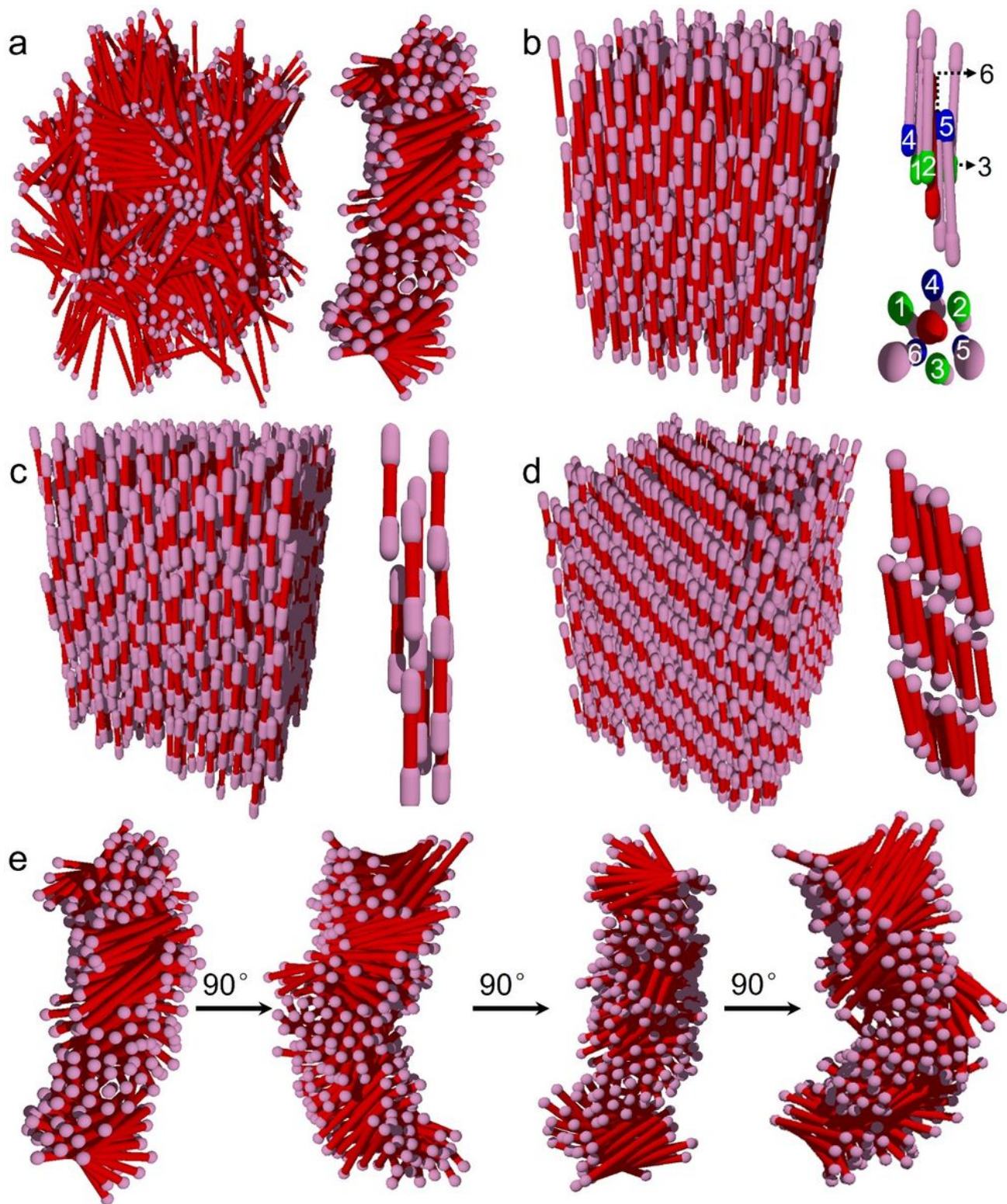


Figure 4

LC phases observed in Brownian dynamics simulations. Simulation results of LC phases assembled from DBCs with (a) $R_D = 1.40$ and $R_L = 0.15$ in N^* phase (right: a double-twisted column extracted from left), (b) $R_D = 1.40$ and $R_L = 0.50$ in N_2 phase (right: side and bottom view of the typical local structure), (c) $R_D = 1.40$ and $R_L = 1.00$ in N_1 phase (right: a cylinder picked out along the z-axis), and (d) $R_D = 1.40$

and $R_L = 1.80$ in the SmA phase (right: a cylinder picked out along the z-axis). (e) Double-twisted structure viewed from different directions.

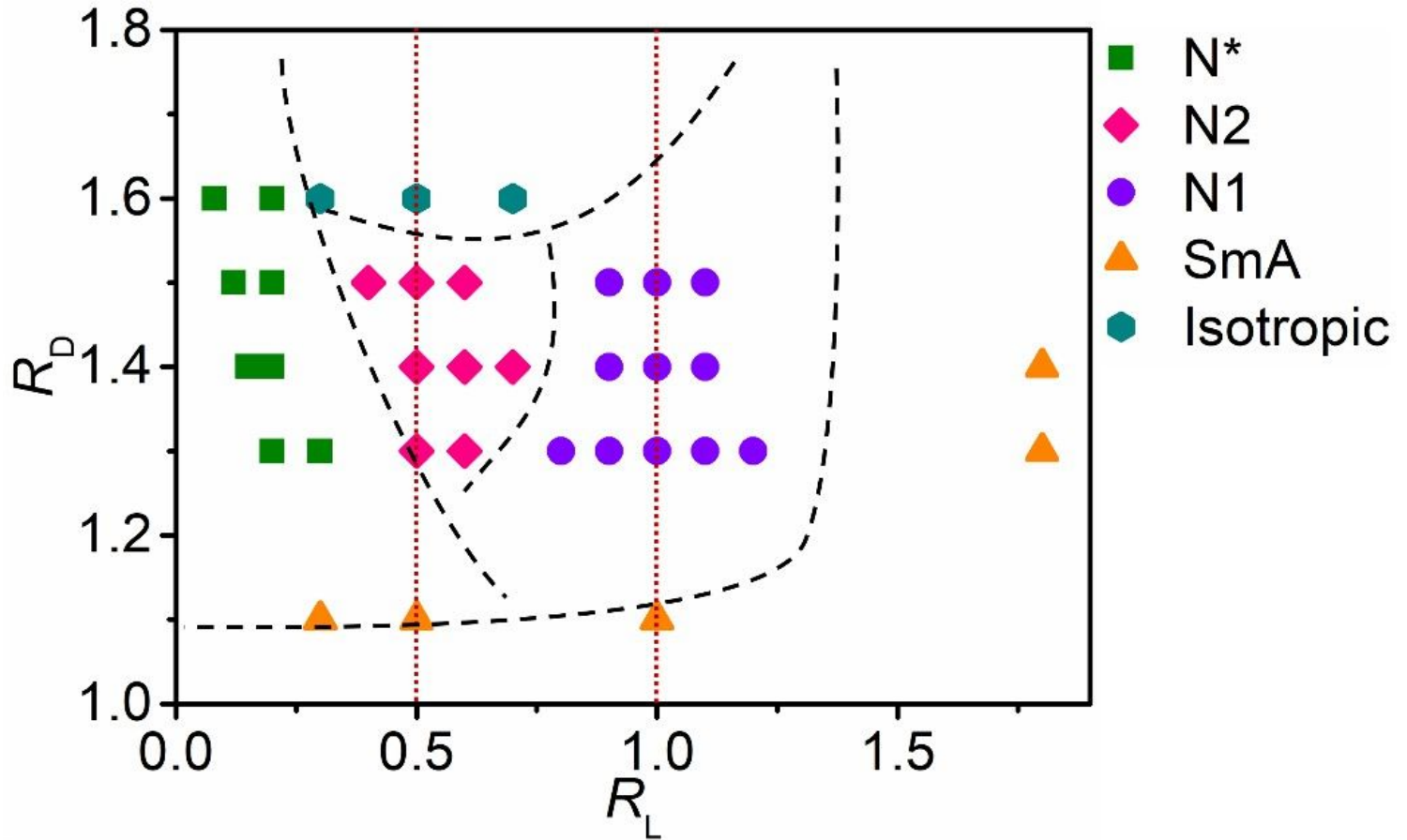


Figure 5

Phase diagram based on simulation results. Computational phase diagram of DBCs as a function of R_D and R_L . The boundary dashed lines are taken from the experimental phase diagram.

Supplementary Files

This is a list of supplementary files associated with this preprint. Click to download.

- [FigureS1.jpg](#)
- [FigureS2.jpg](#)
- [FigureS3.jpg](#)
- [FigureS4.jpg](#)
- [FigureS5.jpg](#)
- [FigureS6.jpg](#)
- [FigureS7.jpg](#)
- [FigureS8.jpg](#)

- [FigureS9.jpg](#)
- [FigureS10.jpg](#)
- [FigureS11.jpg](#)